Indications for a Critical End Point in the Phase Diagram for Hot and Dense Nuclear Matter

Roy A. Lacey

Phys. Rev. Lett. **114**, 142301 — Published 6 April 2015

DOI: 10.1103/PhysRevLett.114.142301

Indications for a critical end point in the phase diagram for hot and dense nuclear matter

Roy A. Lacey[1]

[1]*Depts. of Chemistry & Physics, Stony Brook University, NY 11794*

(Dated: February 19, 2015)

Excitation functions for the Gaussian emission source radii difference ($R^2_{\rm out} - R^2_{\rm side}$) obtained from two-pion interferometry measurements in Au+Au ($\sqrt{s_{NN}}$ = 7.7 − 200 GeV) and Pb+Pb ($\sqrt{s_{NN}}$ = 2.76 TeV) collisions, are studied for a broad range of collision centralities. The observed non-monotonic excitation functions validate the finite-size scaling patterns expected for the deconfinement phase transition and the critical end point (CEP), in the temperature vs. baryon chemical potential (T, μ_B) plane of the nuclear matter phase diagram. A Finite-Size Scaling (FSS) analysis of these data suggests a second order phase transition with the estimates $T^{\rm cep} \sim 165$ MeV and $\mu_B^{\rm cep} \sim 95$ MeV for the location of the critical end point. The critical exponents ($\nu \approx 0.66$ and $\gamma \approx 1.2$) extracted via the same FSS analysis, places this CEP in the 3D Ising model universality class.

PACS numbers: 25.75.Dw

One of the most fundamental phase transitions is that between the hadron gas and the Quark Gluon Plasma (QGP). This Deconfinement Phase Transition (DPT) is usually depicted in the plane of temperature vs. baryon chemical potential (T, μ_B) in the conjectured phase diagram for Quantum Chromodynamics (QCD) [1–4]. The detailed character of this QCD phase diagram is not known and current theoretical knowledge is restricted primarily to the $\mu_B = 0$ axis.

Lattice QCD calculations indicate a crossover quark-hadron transition at small μ_B or high collision energies ($\sqrt{s_{NN}}$) [5, 6]. Similar calculations for much larger μ_B values have been hindered by the well known *sign problem* [7]. However, several model approaches [8–12], as well as mathematical extensions of lattice techniques [13–16], indicate that the transition at larger values of μ_B (lower beam energies [17]) is strongly first order, suggesting the existence of a critical end point (CEP). Pinpointing the location of the phase boundaries and the CEP is central to ongoing efforts to map the QCD phase diagram and to understand the properties of strongly interacting matter under extreme conditions.

The matter produced in ultrarelativistic heavy ion collisions can serve as an important probe for the phase boundaries and the CEP [1–4]. Indeed, a current experimental strategy at the Relativistic Heavy Ion Collider (RHIC) is centered on beam energy scans which enable a search for non-monotonic excitation functions over a broad domain of the (T, μ_B)-plane. The rationale is that the expansion dynamics of the matter produced in these beam energy scans, is strongly influenced by the path of the associated reaction trajectories in the (T, μ_B)-plane. Trajectories which are close to the CEP or cross the coexistence curve for the first order phase transition, are expected to be influenced by anomalies in the dynamic properties of the medium. Such anomalies can drive abrupt changes in the transport coefficients and relaxation rates to give a non-monotonic dependence of the excitation function for the specific viscosity $\frac{\eta}{s}$ *i.e.* the ratio of the shear viscosity η to entropy density s [18–20].

An emitting system produced in the vicinity of the CEP would also be subject to the influence of a divergence in the compressibility of the medium, resulting in a precipitous drop in the sound speed and a collateral increase in the emission duration. Such effects could also give rise to non-monotonic dependencies in the excitation functions for the expansion speed [21, 22], as well as for the difference between the Gaussian emission source radii ($R^2_{\rm out} - R^2_{\rm side}$) extracted from two-pion interferometry measurements [21–25]. This radii difference is linked to the emission duration and consequently, to the compressibility of the medium.

In recent work [26, 27], a striking pattern of viscous damping, compatible with the expected minimum in the excitation function for $\frac{\eta}{s}$ [19, 20] was reported for Au+Au ($\sqrt{s_{NN}}$ = 7.7 − 200 GeV) and Pb+Pb ($\sqrt{s_{NN}}$ = 2.76 TeV) collisions. An excitation function for ($R^2_{\rm out} - R^2_{\rm side}$) extracted for central collisions from the same data sets, also indicated a striking non-monotonic pattern attributed to decay trajectories close to the CEP [27, 28]. Nonetheless, it remains a crucial open question as to whether these non-monotonic patterns are indeed linked to the deconfinement phase transition and the CEP?

In the limit of an infinite volume, the chiral phase transition is characterized by singularities which reflect the divergences in the derivatives of the thermodynamic potential, eg., the specific heat and various susceptibilities (χ). Discontinuities in the first and second derivatives signal the first order and second order phase transitions respectively. These singularities are smeared into finite peaks with modified positions and widths, for more restricted volumes [32, 33].

The correlation length ξ diverges near the transition

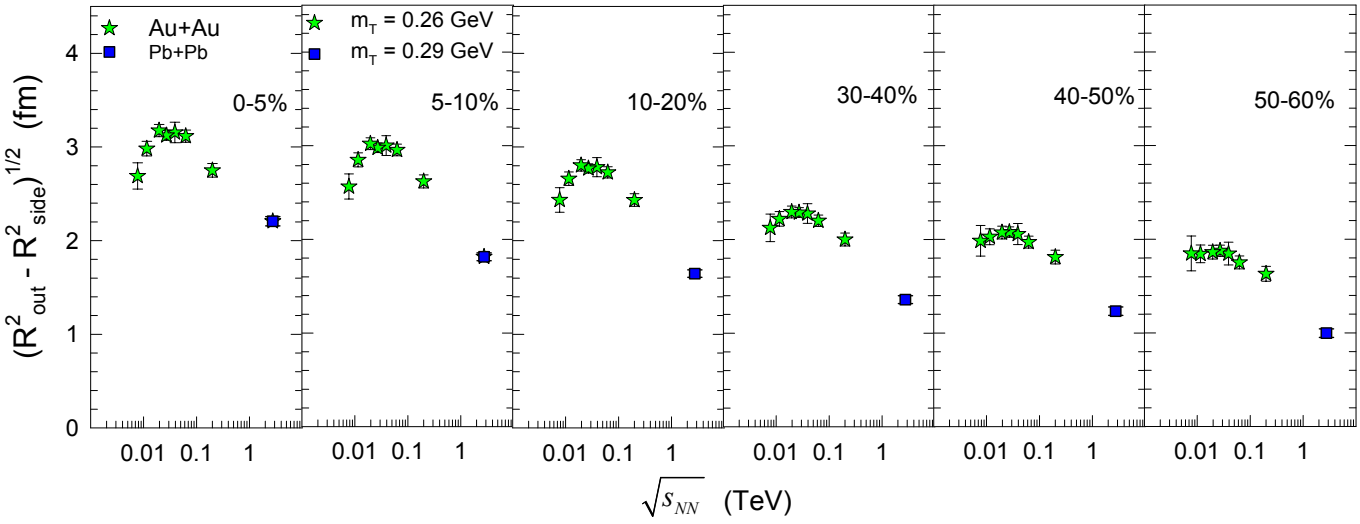

FIG. 1. (Color online) $\sqrt{(R^2_{\rm out} - R^2_{\rm side})}$ vs. $\sqrt{s_{NN}}$ for 0-5%, 5-10%, 10-20%, 30-40%, 40-50% and 50-60% Au+Au and Pb+Pb collisions for $m_T = 0.26$ GeV and 0.29 GeV respectively. The data are taken from Refs. [29–31]

temperature ($T^{\rm cep}$) as $\xi \propto |\tau|^{-\nu}$ for an infinite volume; $\tau = T - T^{\rm cep}$. However, for a system of size L^d (d is the dimension) this second order phase transition is expected to show a pseudocritical point for correlation length $\xi \approx L$. This leads to a characteristic power law volume (V) dependence of the magnitude ($\chi_T^{\rm max}$), width (δT) and peak position (τ_T) of the susceptibility [32];

$$\chi_T^{\rm max}(V) \sim L^{\gamma/\nu}, \quad (1)$$

$$\delta T(V) \sim L^{-\frac{1}{\nu}}, \quad (2)$$

$$\tau_T(V) \sim T^{\rm cep}(V) - T^{\rm cep}(\infty) \sim L^{-\frac{1}{\nu}}, \quad (3)$$

where ν and γ are critical exponents which characterize the divergence of ξ and χ_T respectively. The reduction of the magnitude of $\chi_T^{\rm max}(V)$ ($\chi_{\mu_B}^{\rm max}(V)$), broadening of the transition region $\delta T(V)$ ($\delta\mu_B(V)$) and the shift of $T^{\rm cep}$ ($\mu_B^{\rm cep}$) increases as the volume decreases. A similar set of volume or finite-size dependencies is expected for the first order phase transition, but with unit magnitudes for the critical exponents [32]. Thus, a profitable route for locating the CEP is to search for, and utilize the characteristic finite-size scaling patterns associated with the deconfinement phase transition [32, 33].

In this Letter, we use the Gaussian radii ($R_{\rm out}$ and $R_{\rm side}$) extracted from two-pion interferometry measurements, to first construct non-monotonic excitation functions for $(R^2_{\rm out} - R^2_{\rm side})$ as a function of collision centrality. We then use them to perform validation tests for the characteristic finite-size scaling patterns commonly associated with the deconfinement phase transition and the CEP. We find clear evidence for these scaling properties and use a Finite-Size Scaling (FSS) analysis to extract initial estimates for the (T, μ_B) location of the CEP and the critical exponents associated with it.

The data employed in the present analysis are taken from interferometry measurements by the STAR collaborations for Au+Au collisions spanning the range $\sqrt{s_{NN}} = 7.7 - 200$ GeV [29], and by the ALICE collaboration for Pb+Pb collisions at $\sqrt{s_{NN}} = 2.76$ TeV [30, 31]. The STAR measurements have been reported to be in very good agreement with similar PHENIX measurements obtained at $\sqrt{s_{NN}} = 39, 62.4$ and 200 GeV [27, 28]. The systematic uncertainties for these measurements are also reported to be relatively small [28–31].

The geometric quantities employed in our Finite-Size Scaling analysis were obtained from a Monte Carlo Glauber (MC-Glauber) calculation [34–36], performed for several collision centralities at each beam energy. In each of these calculations, a subset of the nucleons become participants ($N_{\rm part}$) in each collision by undergoing an initial inelastic N+N interaction. The transverse distribution of these participants in the X-Y plane has RMS widths σ_x and σ_y along its principal axes. We define and compute $\bar{R}$, the characteristic initial transverse size, as $1/\bar{R} = \sqrt{(1/\sigma_x^2 + 1/\sigma_y^2)}$ [37]. The systematic uncertainties for $\bar{R}$, obtained via variation of the model parameters, are less than 10% [35, 36].

Figure 1 shows a representative set of excitation functions for $\sqrt{(R^2_{\rm out} - R^2_{\rm side})}$, obtained for the broad selection of centrality cuts indicated. These excitation functions, which are linked to the compressibility of the medium, all show the non-monotonic dependence previously conjectured to reflect reaction trajectories close to the critical end point [27, 28]. They also exhibit several characteristic trends: (i) the magnitude of the peaks decrease with increasing centrality (%) or decreasing transverse size, (ii) the positions of the peaks shift to lower values of $\sqrt{s_{NN}}$ with an increase in centrality and (iii) the width of the distributions grow with centrality. These trends are made more transparent in Fig. 2 where a direct comparison of the excitation functions for $(R^2_{\rm out} - R^2_{\rm side})$

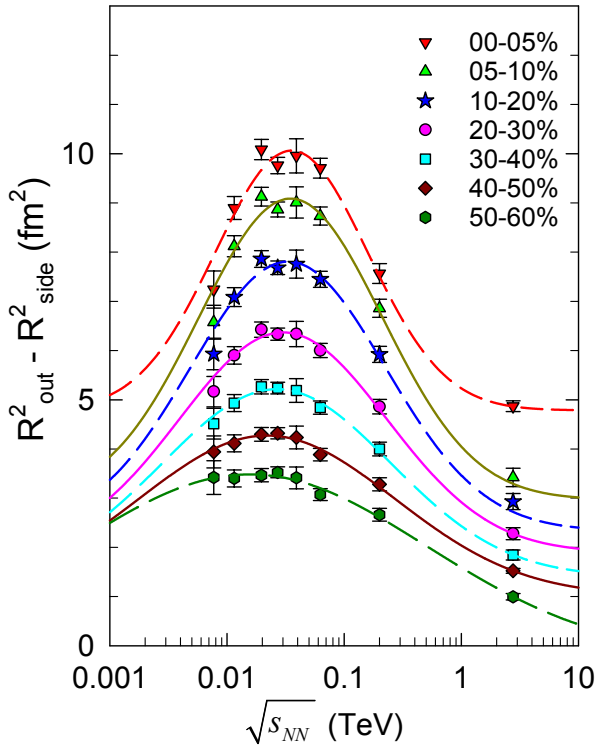

FIG. 2. (Color online) Comparison of $(R^2_{\rm out} - R^2_{\rm side})$ vs. $\sqrt{s_{NN}}$ for several centrality selections as indicated. The data, which are the same as those shown in Fig. 1, are taken from Refs. [29, 30]. The solid and dashed curves represent fits to the combined data sets for each centrality, with the Gaussian fit function $(R^2_{out} - R^2_{side}) = a + b\exp(-0.5[(x-c)/d]^2)$. .

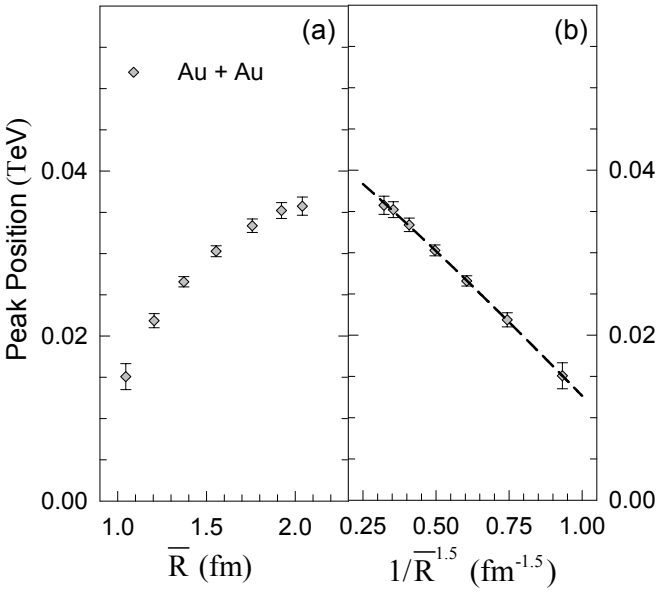

FIG. 3. (Color online) (a) Peak position vs. $\bar{R}$. (b) Peak position vs. $1/\bar{R}^{1.5}$. The peak positions and associated error bars, are obtained from the Gaussian fits shown in Fig. 2. The dashed curve in (b) shows the fit to the data in (a).

is shown. We attribute these qualitative patterns to the finite-size scaling effects expected for the de-confinement phase transition (cf. Eqs. 1 - 3) and employ the excitation functions in a more quantitative Finite-Size Scaling (FSS) analysis as discussed below.

Validation tests for finite-size scaling were carried out for the full set of excitation functions as follows. First, we exploit the phenomenology of thermal models [38–41] for the freeze-out region and associate (T, μ_B) combinations with $\sqrt{s_{NN}}$. Second, we associate $(R^2_{\rm out} - R^2_{\rm side})$ with a susceptibility, given its connection to the isoentropic compressibility (κ_S). The three HBT radii $R_{\rm out}$, $R_{\rm side}$ and $R_{\rm rlong}$, which serve to characterize the space-time dimensions of the emitting source, all show a linear dependence on $\bar{R}$ [27, 28].

Subsequently, a Guassian fit was used to extract the peak positions, and widths of the excitation functions, for different system sizes characterized by the centrality selections indicated in Fig. 2; the magnitude of $(R^2_{\rm out} - R^2_{\rm side})$ was evaluated at the extracted peak positions as well. The solid and dashed curves shown in the figure gives an indication of the quality of these fits.

The extracted fit parameters were tested for the characteristic finite-size scaling patterns associated with the de-confinement phase transition via Eqs. 1 and 3 with $L = \bar{R}$,

$$(R^2_{\rm out} - R^2_{\rm side})^{\rm max} \propto \bar{R}^{\gamma/\nu}, \quad (4)$$

$$\sqrt{s_{NN}}(V) = \sqrt{s_{NN}}(\infty) - k \times \bar{R}^{-\frac{1}{\nu}}, \quad (5)$$

with the aim of obtaining initial estimates for the critical exponents ν and γ and the infinite volume $\sqrt{s_{NN}}(\infty)$ value where the de-confinement phase transition first occurs; k is a constant. Here, $\delta s \equiv (\sqrt{s_{NN}} - \sqrt{s^{cep}_{NN}})/\sqrt{s^{cep}_{NN}}$ gives a measure of the "distance"' to the CEP.

Figure 3 illustrates the finite-size scaling test made for the extracted peak positions ($\sqrt{s_{NN}}(V)$). Panel (a) shows the peak positions vs. $\bar{R}$ while panel (b) shows the same peak positions vs. $1/\bar{R}^{1.5}$. The dashed curve in (b), which represents a fit to the data in (a) with Eq. 5, confirms the expected inverse power law dependence of these peaks on $\bar{R}$. The fit gives the values $\sqrt{s_{NN}}(\infty) = 47.5 \pm 1.5$ GeV and $\nu = 0.67 \pm 0.05$. A similar value for ν was obtained via an analysis of the widths obtained from the Gaussian fits shown in Fig. 2. Note that this value of $\sqrt{s_{NN}}(\infty)$ is compatible with the striking pattern observed in the excitation function for viscous damping [26, 27]. This pattern is akin to that expected for $\frac{\eta}{s}(T, \mu_B)$ close to the CEP [19, 20].

Figure 4 illustrates the results of the finite-size scaling test for $(R^2_{\rm out} - R^2_{\rm side})^{\rm max}$. Panel (a) shows $(R^2_{\rm out} - R^2_{\rm side})^{\rm max}$ vs. $\bar{R}$ while panel (b) shows the same data plotted vs. $\bar{R}^2$. The dashed curve in (b), which represents a fit to the data in (a) with Eq. 4, confirms the expected power law dependence of $(R^2_{\rm out} - R^2_{\rm side})^{\rm max}$

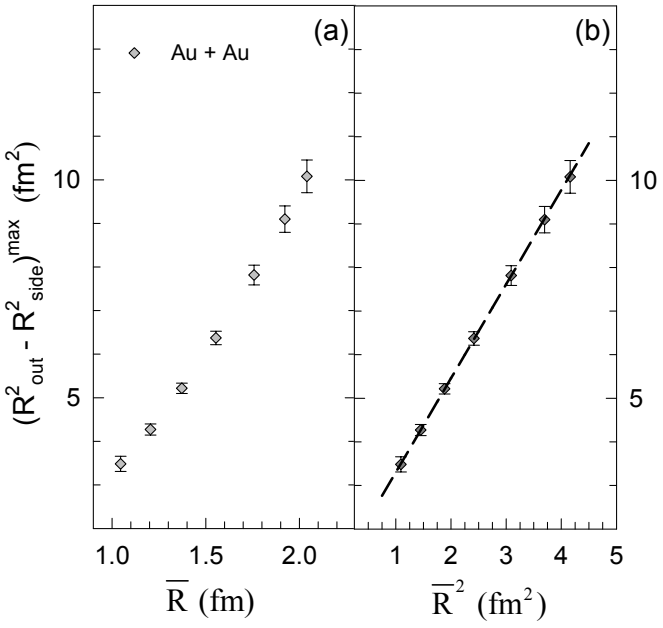

FIG. 4. (Color online) (a) $(R^2_{\rm out} - R^2_{\rm side})^{\rm max}$ vs. $\bar{R}$. (b) $(R^2_{\rm out} - R^2_{\rm side})^{\rm max}$ vs. $\bar{R}^2$. The $(R^2_{\rm out} - R^2_{\rm side})^{\rm max}$ values and associated error bars, are evaluated at the peak positions in Fig. 2. The dashed curve in (b) shows the fit to the data in (a).

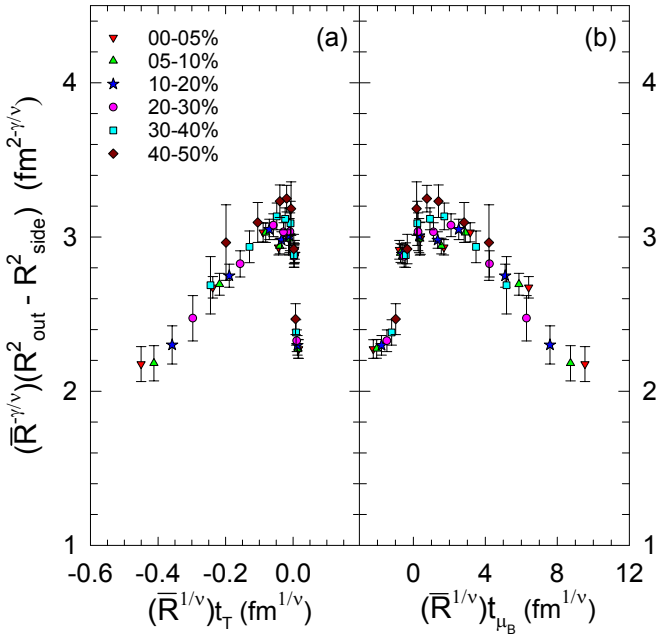

FIG. 5. (Color online) (a) $\bar{R}^{-\gamma/\nu} \times (R^2_{\rm out} - R^2_{\rm side})$ vs. $\bar{R}^{1/\nu} \times t_T$. (b) $\bar{R}^{-\gamma/\nu} \times (R^2_{\rm out} - R^2_{\rm side})$ vs. $\bar{R}^{1/\nu} \times t_{\mu_B}$. The $(R^2_{\rm out} - R^2_{\rm side})$ values are the same as those in Fig. 2. The parametrization for chemical freeze-out [38] is used in conjunction with $\mu_B^{\rm cep}$ and $T^{\rm cep}$ to determine t_T and t_{μ_B}.

on $\bar{R}$. Note that the trend of this dependence is opposite to the inverse power dependence shown in Fig. 3. The fit leads to the estimate $\gamma = 1.15 \pm 0.065$. The indicated uncertainties for ν and γ are derived from the fits.

The magnitudes of the extracted values for the critical exponents $\nu = 0.67 \pm 0.05$ and $\gamma = 1.15 \pm 0.065$, are different from the unit values expected for a first order phase transition [32]. However, they are compatible with the critical exponents for the second order deconfinement phase transition for the 3D Ising model universality class [42, 43]. Consequently, we assign the location of the CEP to the extracted value $\sqrt{s_{NN}}(\infty) = 47.5$ GeV and use the parametrization for chemical freeze-out in Ref. [38] to obtain the estimates $\mu_B^{\rm cep} \sim 95$ MeV and $T^{\rm cep} \sim 165$ MeV for its location in the (T, μ_B)-plane.

A crucial crosscheck for the location of the CEP and its associated critical exponents, is the requirement that finite-size scaling for different transverse sizes, should lead to data collapse onto a single curve for robust values of $T^{\rm cep}$, $\mu_B^{\rm cep}$ and the critical exponents ν and γ;

$$\bar{R}^{-\gamma/\nu} \times (R^2_{\rm out} - R^2_{\rm side}) \text{ vs. } \bar{R}^{1/\nu} \times t_T,$$
$$\bar{R}^{-\gamma/\nu} \times (R^2_{\rm out} - R^2_{\rm side}) \text{ vs. } \bar{R}^{1/\nu} \times t_{\mu_B},$$

where $t_T = (T - T^{\rm cep})/T^{\rm cep}$ and $t_{\mu_B} = (\mu_B - \mu_B^{\rm cep})/\mu_B^{\rm cep}$ are the reduced temperature and baryon chemical potential respectively.

The validation of this crosscheck is illustrated in Fig. 5 where data collapse onto a single curve is indicated for the RHIC excitation functions shown in Fig. 2. The parametrization for chemical freeze-out [38] is used in conjunction with $\mu_B^{\rm cep}$ and $T^{\rm cep}$ to determine the required t_T and t_{μ_B} values from the $\sqrt{s_{NN}}$ values plotted in Fig. 2. Figs. 5(a) and (b) also validate the expected trends for reaction trajectories in the (T, μ_B) domain which encompass the CEP. That is, the scaled values of $(R^2_{\rm out} - R^2_{\rm side})$ peaks at $t_T \approx 0$ and $t_{\mu_B} \approx 0$, and show the collateral fall-off for $t_{T,\mu_B} < 0$ and $t_{T,\mu_B} > 0$.

In summary, we have investigated the centrality dependent excitation functions for the Gaussian emission source radii difference $(R^2_{\rm out} - R^2_{\rm side})$, obtained from two-pion interferometry measurements in Au+Au ($\sqrt{s_{NN}} = 7.7 - 200$ GeV) and Pb+Pb ($\sqrt{s_{NN}} = 2.76$ TeV) collisions, to search for the CEP in the nuclear matter phase diagram. The observed centrality dependent non-monotonic excitation functions, validate characteristic finite-size scaling patterns which are consistent with a deconfinement phase transition and the critical end point. An initial Finite-Size Scaling analysis of these data suggests a second order phase transition with $T^{\rm cep} \sim 165$ MeV and $\mu_B^{\rm cep} \sim 95$ MeV for the location of the critical end point. The critical exponents ($\nu = 0.67 \pm 0.05$ and $\gamma = 1.15 \pm 0.065$) extracted in the same FSS analysis, places the CEP in the 3D Ising model universality class. Further detailed studies at RHIC are crucial to make a more precise determination of the location of the CEP and the associated critical exponents, as well as to confirm these observations for other collision systems.

ACKNOWLEDGMENTS

The author thanks J. Jia, E. Fraga, B. Schenke, L. Sobotka and R. Venugopalan for valuable discussions, and for pointing out several important references. This research is supported by the US DOE under contract DE-FG02-87ER40331.A008.

[1] N. Itoh, Prog. Theor. Phys. **44**, 291 (1970).
[2] E. V. Shuryak, CERN-83-01 (1983).
[3] M. Asakawa and K. Yazaki, Nucl. Phys. **A504**, 668 (1989).
[4] M. A. Stephanov, K. Rajagopal, and E. V. Shuryak, Phys. Rev. Lett. **81**, 4816 (1998), hep-ph/9806219.
[5] Y. Aoki, G. Endrodi, Z. Fodor, S. Katz, and K. Szabo, Nature **443**, 675 (2006), hep-lat/0611014.
[6] T. Bhattacharya, M. I. Buchoff, N. H. Christ, H. T. Ding, R. Gupta, et al., Phys.Rev.Lett. **113**, 082001 (2014), 1402.5175.
[7] P. de Forcrand, PoS **LAT2009**, 010 (2009), 1005.0539.
[8] J. Berges and K. Rajagopal, Nucl.Phys. **B538**, 215 (1999), hep-ph/9804233.
[9] Y. Hatta and T. Ikeda, Phys.Rev. **D67**, 014028 (2003), hep-ph/0210284.
[10] M. A. Stephanov, Prog.Theor.Phys.Suppl. **153**, 139 (2004), hep-ph/0402115.
[11] M. Asakawa and C. Nonaka, Nucl.Phys. **A774**, 753 (2006), nucl-th/0509091.
[12] S. Ejiri, Phys.Rev. **D78**, 074507 (2008), 0804.3227.
[13] Z. Fodor and S. Katz, JHEP **0404**, 050 (2004), hep-lat/0402006.
[14] A. Li, A. Alexandru, and K.-F. Liu, Phys.Rev. **D84**, 071503 (2011), 1103.3045.
[15] K. Nagata, K. Kashiwa, A. Nakamura, and S. M. Nishigaki (2014), 1410.0783.
[16] P. de Forcrand, J. Langelage, O. Philipsen, and W. Unger, Phys.Rev.Lett. **113**, 152002 (2014), 1406.4397.
[17] The baryon chemical potential increases with the decrease in the beam energy while the chemical freeze-out temperature increases with increase in beam energy [38].
[18] R. A. Lacey, N. Ajitanand, J. Alexander, P. Chung, W. Holzmann, et al., Phys.Rev.Lett. **98**, 092301 (2007), nucl-ex/0609025.
[19] L. P. Csernai, J. Kapusta, and L. D. McLerran, Phys.Rev.Lett. **97**, 152303 (2006), nucl-th/0604032.
[20] R. A. Lacey et al. (2007), 0708.3512.
[21] C. Hung and E. V. Shuryak, Phys.Rev.Lett. **75**, 4003 (1995), hep-ph/9412360.
[22] D. H. Rischke and M. Gyulassy, Nucl.Phys. **A608**, 479 (1996), nucl-th/9606039.
[23] S. Pratt, Phys.Rev.Lett. **53**, 1219 (1984).
[24] S. Chapman, P. Scotto, and U. W. Heinz, Phys.Rev.Lett. **74**, 4400 (1995), hep-ph/9408207.
[25] U. A. Wiedemann, P. Scotto, and U. W. Heinz, Phys.Rev. **C53**, 918 (1996), nucl-th/9508040.
[26] R. A. Lacey, A. Taranenko, J. Jia, D. Reynolds, N. Ajitanand, et al., Phys. Rev. Lett. **112**, 082302 (2014).
[27] R. A. Lacey (2014), 1408.1343.
[28] A. Adare et al. (PHENIX Collaboration) (2014), 1410.2559.
[29] L. Adamczyk et al. (STAR Collaboration) (2014), 1403.4972.
[30] K. Aamodt et al. (ALICE Collaboration), Phys.Lett. **B696**, 328 (2011), 1012.4035.
[31] A. Kisiel (ALICE Collaboration), PoS **WPCF2011**, 003 (2011).
[32] M. Ladrem and A. Ait-El-Djoudi, Eur.Phys.J. **C44**, 257 (2005), hep-ph/0412407.
[33] L. Palhares, E. Fraga, and T. Kodama, J.Phys. **G38**, 085101 (2011), 0904.4830.
[34] M. L. Miller, K. Reygers, S. J. Sanders, and P. Steinberg, Ann. Rev. Nucl. Part. Sci. **57**, 205 (2007).
[35] R. A. Lacey, R. Wei, N. Ajitanand, and A. Taranenko, Phys.Rev. **C83**, 044902 (2011), 1009.5230.
[36] A. Adare et al. (PHENIX Collaboration) (2013), 1310.4793.
[37] R. Bhalerao, J.-P. Blaizot, N. Borghini, and J.-Y. Ollitrault, Phys.Lett. **B627**, 49 (2005), nucl-th/0508009.
[38] J. Cleymans, H. Oeschler, K. Redlich, and S. Wheaton, J.Phys. **G32**, S165 (2006), hep-ph/0607164.
[39] A. Andronic, P. Braun-Munzinger, and J. Stachel, Acta Phys.Polon. **B40**, 1005 (2009), 0901.2909.
[40] F. Becattini, M. Bleicher, T. Kollegger, M. Mitrovski, T. Schuster, et al., Phys.Rev. **C85**, 044921 (2012), 1201.6349.
[41] A. N. Tawfik, Int.J.Mod.Phys. **A29**, 1430021 (2014), 1410.0372.
[42] E. V. Andrea Pelissetto, Phys.Rept. **368**, 549 (2002), 0012164.
[43] H. Kleinert, Phys.Rev.D **60**, 085001 (1999).